



Efficient solar-driven degradation of a tire wear pollutant using floating K-doped g-C₃N₄ photocatalyst in secondary municipal wastewater[☆]

Bouthaina Aoudi, Julide Kahkeci, Isaac Sánchez-Montes, Yaman Boluk^{*},
Mohamed Gamal El-Din^{**}

Department of Civil and Environmental Engineering, University of Alberta, 9211 -116 Street NW, Edmonton, Alberta T6G 1H9, Canada

ARTICLE INFO

Editor: B. Van der Bruggen

Keywords:

Photocatalysis
Potassium-doping
Graphitic Carbon Nitride
Expanded Perlite
Tire Wear Pollutant
Wastewater Treatment

ABSTRACT

Graphitic carbon nitride (g-C₃N₄) is a promising photocatalyst for solar-driven degradation of contaminants of emerging concern (CECs). However, its powdered form complicates recovery for large-scale applications in water treatment. In this study, we developed potassium-doped g-C₃N₄ (KCN) supported on expanded perlite (EP), a non-toxic volcanic glass, to address these recovery challenges. KCN was synthesized *in situ* by adding varying amounts of KOH to urea and EP, followed by calcination. The EP/KCN composites were characterized and tested for the degradation of 1,3-diphenyl guanidine (DPG), a tire wear pollutant. SEM images showed that KCN coverage increased with higher urea loading on EP, with EP/KCN20 (20:1 urea to EP, 1 wt% KOH) having nearly complete surface coverage. FT-IR spectra confirmed stronger C-N and C=N stretching vibrations with increased KCN content, confirming the successful incorporation of KCN into the composite. XRD patterns displayed distinct KCN peaks at higher loadings, while PL analysis suggested slightly reduced charge recombination in the EP/KCN20 composite, indicating enhanced photocatalytic efficiency. Furthermore, EP/KCN20 achieved 96.1 % degradation of DPG under simulated solar exposure in 5 h, with over 80 % efficiency maintained across four consecutive cycles. The composite also demonstrated robust performance under more complex conditions, including natural solar light and in DPG-spiked secondary municipal wastewater, with a cost of 5.57 USD/m³. These findings highlight the potential of the EP/KCN composite as a scalable, cost-effective solution for the removal of CECs from wastewater, driven by renewable solar energy.

1. Introduction

Advanced oxidation processes (AOPs) are promising, efficient, and eco-friendly technologies that utilize strong oxidizing species for the rapid and effective degradation of organic pollutants from water and wastewater [1,2]. Photocatalysis, a widely recognized AOP, has proven highly effective for this purpose [3,4]. Among various photocatalysts, graphitic carbon nitride (CN) stands out due to its sustainability, non-toxic nature, abundance, and simple synthesis from inexpensive nitrogen-rich precursors such as urea and melamine [5–7]. CN is typically prepared through the pyrolysis of these precursors at high temperatures, either in air or under inert atmospheres. Previous studies have shown that using nitrogen gas during pyrolysis offers several advantages

over air [8,9]. This inert environment during synthesis prevents oxidation and promotes the formation of a more stable and homogeneous CN structure [10,11]. It also prevents unwanted side reactions from occurring, preserving the integrity of CN [12].

CN has attracted significant attention for its photocatalytic applications, including the degradation of organic pollutants, hydrogen production, and CO₂ reduction [13,14]. Its unique two-dimensional layered structure, narrow band gap, and tunability make it an ideal candidate for efficient photocatalytic reactions [15]. Despite its promising properties, bare CN faces several limitations that hinder its photocatalytic efficiency. These include poor electron-hole (e⁻/h⁺) separation, low surface area, and restricted visible light absorption, all of which contribute to reduced performance in photocatalytic reactions [5,16]. Recent efforts

[☆] This article is part of a special issue entitled: 'AOP for CEC removal' published in Separation and Purification Technology.

^{*} Corresponding author at: 7-273 Donadeo Innovation Centre for Engineering, Department of Civil and Environmental Engineering, University of Alberta, 9211 -116 Street NW, Edmonton, Alberta T6G 1H9, Canada.

^{**} Corresponding author at: 7-285 Donadeo Innovation Centre for Engineering, Department of Civil and Environmental Engineering, University of Alberta, 9211 -116 Street NW, Edmonton, Alberta T6G 1H9, Canada.

E-mail addresses: yaman@ualberta.ca (Y. Boluk), mgamalel-din@ualberta.ca (M.G. El-Din).

<https://doi.org/10.1016/j.seppur.2025.132523>

Received 8 November 2024; Received in revised form 21 February 2025; Accepted 12 March 2025

Available online 14 March 2025

1383-5866/© 2025 The Author(s). Published by Elsevier B.V. This is an open access article under the CC BY-NC-ND license (<http://creativecommons.org/licenses/by-nc-nd/4.0/>).

to enhance the performance of CN have focused on elemental doping, which introduces defects and vacancies that act as active sites for photocatalytic reactions [17–19]. Potassium (K) doping, in particular, is a simple yet highly effective method that significantly improves the properties of CN by reducing charge recombination rates and increasing reactive oxygen species (ROS) generation, thus enhancing the overall photocatalytic activity [20–22]. A previous study by our research group extensively examined the impact of K-doping on the degradation of DPG, demonstrating significant improvements in photocatalytic efficiency compared to bare CN. These enhancements were attributed to better charge separation, increased ROS generation, and improved adsorption [23]. Building on these findings, this study focuses on the implementation of K-doped CN on a solid substrate to improve stability and enable large-scale application.

In addition to the limited performance of bare CN, the practical application of CN and most photocatalysts in real wastewater treatment is often constrained by their powder form. The powder form suffers from aggregation, as well as difficulties in separation and reuse. To address these issues, recent strategies have focused on templating photocatalysts onto various substrates, including glass beads, perlite, silica, and biopolymers such as chitosan and cellulose. These methods enhance the stability of photocatalysts and facilitate their practical application in wastewater treatment systems [24–26]. Floating substrates offer numerous advantages, including direct exposure to solar irradiation and enhanced oxygenation at the air/water interface, which significantly improves ROS formation. Most importantly, these substrates are easy to recover and reuse after treatment [27–29].

Expanded perlite (EP) is a lightweight volcanic material that expands up to 20 times its original volume when heated above 800 °C, creating a porous structure with low density and buoyancy. Composed of over 70 % silica, EP is chemically inert, pH-neutral, and fire-resistant, ensuring stability under various conditions [30,31]. Its abundance, low cost, and ease of separation make it an ideal support material for photocatalytic applications, especially in large-scale wastewater treatment [32–34]. The porous structure provides active sites for trapping charge carriers, reducing e^-/h^+ recombination, and enhancing photocatalytic efficiency, while its buoyancy allows for easy post-reaction separation.

Several research studies have investigated the use of CN supported on the EP surface (EP/CN composites) for environmental remediation, including the photocatalytic inactivation of *Microcystis aeruginosa* and *Escherichia coli* and MS2 [35–37]. These composites have also been applied in the photocatalytic degradation of common organic contaminants. For example, Liu et al. utilized a Z-scheme $\text{FeMo}_3\text{O}_x/\text{CN}$ composite on EP to degrade tetracycline via a Fenton-like process [38]. Similarly, Hai Bang Truong et al. employed mesoporous EP/KCN in combination with hydrogen peroxide for natural organic matter removal [36], while Sun et al. investigated the activation of peroxymonosulfate using $\text{CN}/\text{CuFe}_2\text{O}_4$ supported on EP for the removal of sulfamethazine [39]. However, these methods often require additional chemicals and specific conditions, such as acidic pH, complicating their practical applications.

In contrast, solar-driven catalysis offers a more sustainable approach by utilizing renewable solar energy under milder, environmentally friendly conditions. Despite its advantages, the application of EP/KCN in solar-driven catalysis remains limited, with most research focusing on the degradation of simpler pollutants like dyes. For instance, Chen et al. [40] and Zhang et al. [41] both studied the use of this composite for the degradation of rhodamine B. To date, no studies have investigated the application of EP/KCN composites for the degradation of more recalcitrant contaminants, such as tire wear particles, nor have they explored their use in complex real wastewater matrices.

This research addresses this critical gap in wastewater treatment by exploring EP/KCN composites for the degradation of 1,3-diphenylguanidine (DPG), a tire wear pollutant. Tire wear particles are composed of various components, including natural and synthetic rubbers, carbon black, plasticizers (e.g., phthalates), vulcanizing agents (e.g., sulfur),

accelerators (e.g., benzothiazoles and 1,3-diphenylguanidine), and heavy metals [42]. These additives and contaminants, many of which are toxic and persistent in the environment, pose significant risks to aquatic ecosystems and human health. DPG, a vulcanization accelerator widely used in tire manufacturing, is particularly concerning due to its persistence in the environment and leachability into water bodies, contaminating road runoff, rivers, and wastewater [43–45]. Despite its frequent detection and toxicological impact, studies on its effective removal remain limited [46–48].

This study systematically investigates the degradation of DPG using EP/KCN while examining key experimental parameters, including the urea-to-EP ratio, catalyst amount, and EP particle size. In addition, a simple yet highly effective enhancement method is introduced by incorporating an aluminum reflective surface beneath the reactor to increase light absorption and improve overall performance. The stability and reusability of the most effective composite are also evaluated over multiple cycles. Finally, a preliminary assessment of the proposed system to treat DPG in real secondary effluent from a municipal wastewater treatment plant (WWTP) is discussed. To our best knowledge, this is the first study to demonstrate the use of a KCN templated on floating EP under natural solar irradiation for the degradation of an emerging contaminant in wastewater, providing a solid foundation for future research in this area.

2. Experimental

2.1. Materials

Expanded Perlite (EP) was purchased from Miracle-Gro® with a density of 50.5 kg/m³. 1,3-diphenylguanidine (DPG) ($\text{DPG} ((\text{C}_6\text{H}_5\text{NH})_2\text{C} = \text{NH}, 97.0 \%)$), urea (99.0 %), potassium hydroxide (KOH, >85.0 %), 1,4-benzoquinone (BQ), isopropanol (IPA, ≥99.5 %), ammonium oxalate monohydrate (AO, ≥99.0 %), methanol (HPLC grade), and acetonitrile (HPLC grade) were purchased from Sigma-Aldrich. 5,5-dimethyl-1-pyrrolidine oxide (DMPO) was acquired from ACROS. All chemicals were used as received, and all solutions were prepared using ultrapure water (Millipore Synergy® UV, $\rho \geq 18.2 \text{ M}\Omega \text{ cm}$). Secondary municipal effluent (pH 8.20 and conductivity of 1.60 mS/cm) was collected from a local WWTP in Edmonton, Canada.

2.2. Preparation of EP/KCN composites

EP particles were sieved using 10, 18, and 30 mesh screens to obtain three different sizes. These particles were cleaned with deionized water, soaked overnight to collect only the floating particles, and then dried in an oven at 60 °C. For composite preparation, 1 g of EP was combined with varying amounts of urea (5, 10, 20, and 30 g) in 40 mL of deionized water. KOH was added at 1 wt% of the urea mass, following the method reported in a previous work [23]. The EP and urea mixture were sonicated for 1 h to ensure uniform dispersion and then dried completely overnight. The dried mixtures were transferred to ceramic crucibles and heated in a muffle furnace at 550 °C for 2 h, with a ramp rate of 5 °C/min. After cooling to room temperature, the composites were thoroughly washed and centrifuged multiple times to remove excess KCN and impurities. The resulting composites (EP/KCN_x) were labeled according to their urea-to-EP mass ratios, where x is 5, 10, 20, and 30.

2.3. Characterization techniques

The morphology was examined using Scanning Electron Microscopy (SEM) with a Zeiss Sigma 300 VP-FESEM. Crystal structures were characterized by powder X-ray diffraction (XRD) with a Bruker D8 Discover. Fourier-transform infrared (FTIR) spectroscopy was performed with a Nicolet 6700 spectrometer. Elemental composition and distribution were analyzed using CHNS, EDX, and elemental mapping. CHNS analysis was performed with a Thermo Flash 2000 CHNS-O

analyzer, where the C, H, N, and S content were determined by combusting the samples in an O-rich environment, with the resulting gases being separated and quantified. Calibration was performed with an organic analytical standard (OAS), ensuring an $R^2 \geq 0.999$, with accuracy verified every four runs ($\pm 0.3\%$ deviation). Chemical states were analyzed using X-ray Photoelectron Spectroscopy (XPS) on a Kratos AXIS Ultra. The specific surface area was determined by Brunauer-Emmett-Teller (BET) using N_2 adsorption-desorption isotherms on an Autosorb-iQ. Photoluminescence (PL) spectra were recorded at 355 nm excitation using Cary Eclipse, Varian spectrofluorometer. The bandgap energy was derived from Diffuse Reflectance Spectroscopy (DRS) using an Agilent Cary 5000 UV-VIS-NIR spectrometer. The bandgap energies of the composites were determined using UV-Vis DRS and analyzed with the Tauc plot method, as described by the following equation:

$$(\alpha h\nu)^{\frac{1}{\gamma}} = B(h\nu - E_g)$$

where α is the adsorption coefficient to the photon, h is Planck's constant, ν is the frequency of light, B is a constant, E_g is the bandgap, and γ is a constant that depends on the nature of the electron transition (1/2 or 2 for the direct and indirect transition bandgaps, respectively). For CN-based materials, γ is usually reported as 2 [49].

2.4. Analytical methods

The Quantitative analysis of DPG (1 mg/L) was conducted using Agilent 1260 Infinity II high-performance liquid chromatography with diode array detection (HPLC-DAD), as reported in a previous study [50]. DPG peak was recorded at 254 nm. For lower concentrations of DPG (100 $\mu\text{g/L}$) in spiked secondary effluent, ultrahigh-performance liquid chromatography coupled with triple quadrupole mass spectrometry (UHPLC/QqQ-MS) was used [4].

To identify intermediate compounds produced during the photocatalytic degradation of DPG, ultra-performance liquid chromatography coupled with time-of-flight mass spectrometry (UPLC-TOFMS) using a Synapt G2 system (Waters) was employed. Chromatographic separation followed the method described in previous studies [51,52]. TOFMS operated in positive electrospray ionization (ESI+) mode, conducting MS scans from 50 to 500 (m/z) in high-resolution mode. MassLynx software managed data acquisition, and spectral data was processed using TargetLynx.

ROS were detected using scavenger tests and electron paramagnetic resonance (EPR). AO, BQ, and IPA were used as scavengers for holes (h^+), superoxide radicals ($O_2^{\cdot-}$), and hydroxyl radicals ($\cdot\text{OH}$), respectively. EPR spectra were recorded using a Bruker A300-10/12 EPR spectrometer with 1 mL of 50 mM DMPO in water and methanol for spin-trapping of $\cdot\text{OH}$ and $O_2^{\cdot-}$, respectively.

2.5. Photocatalytic experiments

The prepared composites were tested for the photocatalytic degradation of DPG using a solar simulator (SS200AAA, Photon Emission Tech, USA) equipped with a 1000 W arc lamp and a fixed irradiance of 100 mW/cm^2 , controlled by SolarSimulator.vi software. A specific amount of EP/KCN (0.02, 0.06, and 0.1 g) was added to a crystallizing dish (60 mm diameter \times 35 mm height) containing 50 mL of DPG solution (1 mg/L) prepared with ultrapure water (pH \sim 7). The solvent height was approximately 1.8 cm. The mass used is equivalent to a small number of perlites (Fig. S1), occupying only a limited area of the surface to facilitate effective contaminant-catalyst interaction. To enhance light reflection and maximize catalyst exposure, aluminum foil was placed beneath the dish. The solution was stirred continuously at a low speed (100 rpm) in the dark for 1 h to establish adsorption/desorption equilibrium before switching on the solar simulator, ensuring consistent contaminant-catalyst contact. Samples were collected at fixed time intervals and filtered through a 0.2 μm nylon membrane filter before

analysis. The system was also tested using secondary effluent from a municipal WWTP spiked with DPG (100 $\mu\text{g/L}$) and natural solar irradiation. The experiment was conducted outdoors on a clear, sunny day from 12:00 pm to 17:00 local time with 5.06 kWh/m^2 [53] (Edmonton, Canada – 53.5268° N, 113.5291° W).

3. Results and discussion

3.1. Characterization of composite photocatalysts

SEM images of bare EP (Fig. 1a) reveal a porous, rough surface with an average particle size of approximately 1.3 μm , offering sufficient surface area for deposition. Upon the deposition of KCN, the pores on the EP surface are gradually filled, increasing the surface coverage (Fig. 1b). The EP/KCN5 shows limited KCN deposition, whereas EP/KCN20 and EP/KCN30 composites display nearly complete surface coverage, resulting in a more uniform and dense coating (Fig. S2). Higher KCN loading not only improves surface coverage but also increases the exposure of KCN to the contaminant solution, which could enhance the photocatalytic activity of the composite.

Elemental CHNS analysis was used to estimate the surface coverage of KCN on the EP surface in EP/KCN, as perlite is primarily inorganic. The theoretical KCN loadings for EP/KCN5, EP/KCN10, EP/KCN20, and EP/KCN30 were calculated to be 6.9 %, 14.2 %, 22.6 %, and 25.0 %, respectively (Table 1). The actual KCN deposition on each composite was determined by measuring the total weight of EP/KCN, subtracting the weight of bare EP (adjusted for thermal treatment losses), and accounting for any excess KCN that did not adhere to the EP. The actual KCN coverage closely matched the theoretical values, with a deviation of approximately 4.0 %.

To further validate these results, EDX analysis was conducted to confirm the presence of key elements (Figs. S3 and S4), while elemental mapping was employed to assess the spatial distribution of KCN on the EP surface (Fig. 1c). The mapping results confirmed the successful deposition of KCN onto the EP, with KCN clusters primarily composed of C and N, while the EP support showed a high concentration of Al, Si, and O. K was detected throughout the surface, reflecting its dual presence as an oxide in EP and as a dopant in KCN. EDX analysis supported these observations, revealing that the EP surface is mainly composed of Si (31.4 %), Al (5.5 %), and O (42.6 %), along with some K (5.8 %) (Fig. S3). These results align with the known composition of perlite, which is typically rich in silica, alumina, and other metal oxides [54]. The KCN clusters were predominantly composed of C (31.5 %) and N (52.9 %), with some K (7.1 %) (Fig. S4).

FT-IR spectroscopy was employed to characterize the surface functional groups of bare EP (Fig. S5) and EP/KCN composites (Fig. 2a). The spectra of all EP/KCN composites displayed characteristic vibrational peaks associated with EP, including the Si-O-Si stretching band at 800–1100 cm^{-1} (the yellow strip in Fig. 2a) and the Si-O stretching band of the Si-O-Al bond at around 780 cm^{-1} [55]. The intensity of these peaks decreased with increasing KCN loading, with EP/KCN5 showing the highest intensity. The presence of KCN in the composites is confirmed by distinctive peaks related to melem units, including C-N stretching vibrations at 1249, 1360, and 1465 cm^{-1} , as well as C=N stretching peaks at 1565 and 1630 cm^{-1} (gray strip in Fig. 2a) [56]. These peaks were more pronounced with increasing KCN content, with the most significant peaks observed in EP/KCN30.

The crystalline structures were analyzed using XRD patterns. As shown in Fig. S6, EP exhibits a broad amorphous aluminosilicate gel phase between $2\theta = 20^\circ$ and 35° [57], with a peak around 26.5° , likely corresponding to quartz. KCN displayed characteristic CN peaks at $2\theta \approx 13.4^\circ$ and 27.6° , attributed to in-plane structural packing and interlayer stacking (Fig. 2b) [58]. In EP/KCN composites, these CN peaks were less pronounced, with the peak at 13° almost invisible, likely due to overlapping with the broad amorphous signal of EP or reduced crystalline order in CN. As KCN content increased from EP/KCN5 to EP/KCN30,

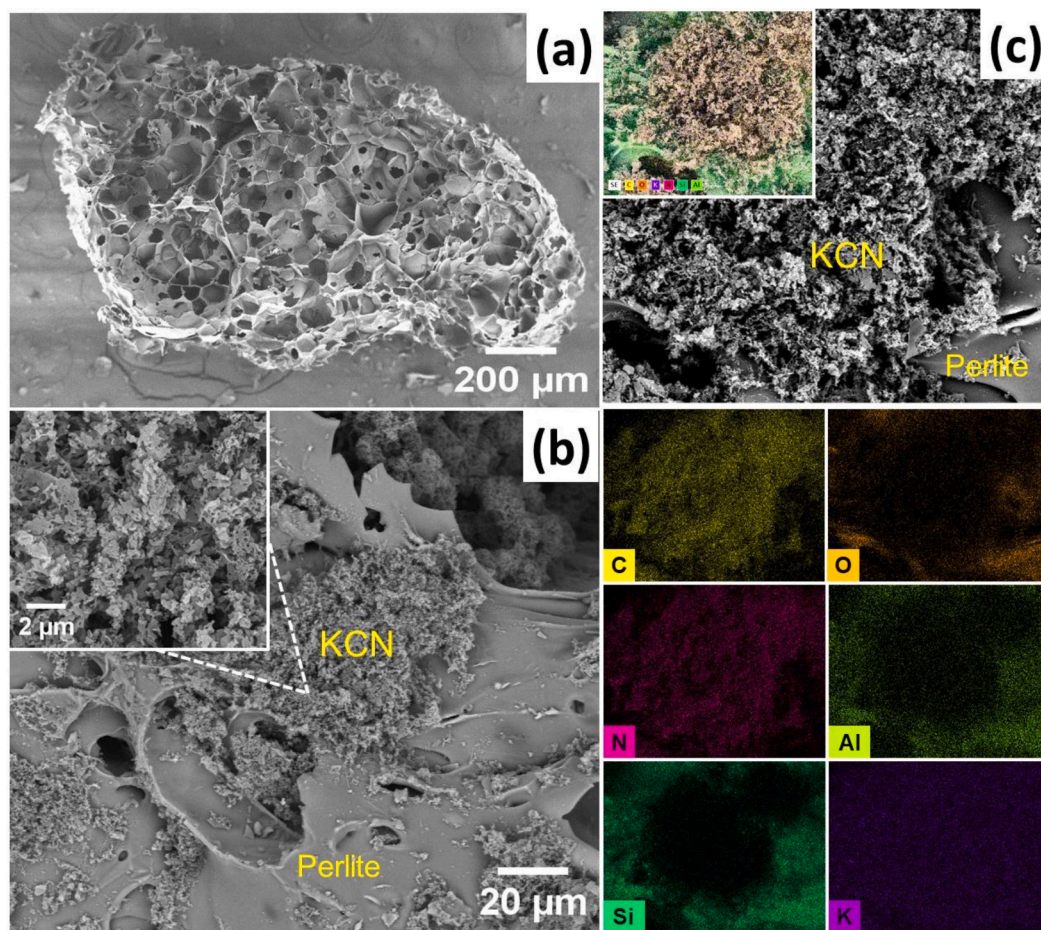


Fig. 1. SEM images of (a) bare EP, (b) EP/KCN20 with an inset magnified at KCN, and (c) elemental mapping of EP/KCN20 showing the elements present.

Table 1
Properties of different prepared composites.

Sample	Weight ratio of urea to EP	% KCN	Bandgap (eV)	Surface Area (m ² /g)	R ²
EP	0	0.0	—	1.647	0.994
EP/ KCN5	5	6.9	2.46	3.070	0.995
EP/ KCN10	10	14.2	2.56	3.885	0.997
EP/ KCN20	20	22.6	2.49	4.739	0.981
EP/ KCN30	30	25.0	2.54	4.756	0.999
KCN	0	100	2.50	4.644	0.999

peak intensity slightly increased but remained weak, suggesting lower crystallinity or reduced CN content in the composites.

The optical properties were studied using UV-DRS absorbance measurements. As shown in Fig. 2c, both the EP/KCN composites and bare KCN exhibit a similar absorption edge around 400 nm, indicating comparable light absorption behavior in this region. Beyond this point, a gradual decrease in absorbance is observed with increasing KCN content. Since EP itself does not have significant absorbance in this region (Fig. S7), the observed decrease is likely attributed to interactions between EP and KCN. These interactions may lead to increased light scattering due to irregular stacking of KCN or partial coverage of KCN by EP, both of which can affect light transmission through the composite [59].

The bandgap values of the EP/KCN composites were analyzed using

the Tauc plot, to better understand the effect of EP on the optical properties (Fig. S8). The bandgap of the EP/KCN composites ranged from 2.46 eV to 2.56 eV, which is very close to the bandgap of bare KCN (2.50 eV). This suggests that while EP might affect the light absorption behavior of the composites slightly, it does not significantly alter the electronic structure of KCN, implying that the bandgap remains largely unaffected by the presence of EP in the composites [60].

The charge carrier recombination behavior of EP/KCN composites was investigated using PL spectroscopy (Fig. 2d). All composites revealed a peak around 460 nm, with a slight redshift from the peak of pure KCN at 445 nm, likely due to interactions between EP and KCN. The PL intensity followed the trend EP/KCN5 > EP/KCN10 > EP/KCN30 > EP/KCN20, indicating that higher KCN content generally reduced the PL intensity, except EP/KCN20, which showed the lowest PL intensity. This low intensity, possibly suggests increased charge carrier separation and decreased recombination rates of e^-/h^+ pairs. A similar trend has been reported by other researchers, indicating that increasing the photocatalyst to EP weight ratio reduces charge recombination and enhances photocatalytic performance, though only up to an optimal ratio [61]. This phenomenon may be attributed to excessive catalyst loading, leading to aggregation or limited charge separation [62].

The BET surface area of the composites was analyzed and presented in Table 1. The specific surface area of bare EP was measured at 1.647 m²/g. As KCN was loaded onto EP increased, the specific surface area of the composites progressively increased, with EP/KCN30 showing the highest surface area of 4.756 m²/g. This increase likely resulted from the formation of porous KCN layers on the EP surface, contributing to higher surface area without fully blocking the underlying EP pores. These findings are consistent with previous studies that investigated the

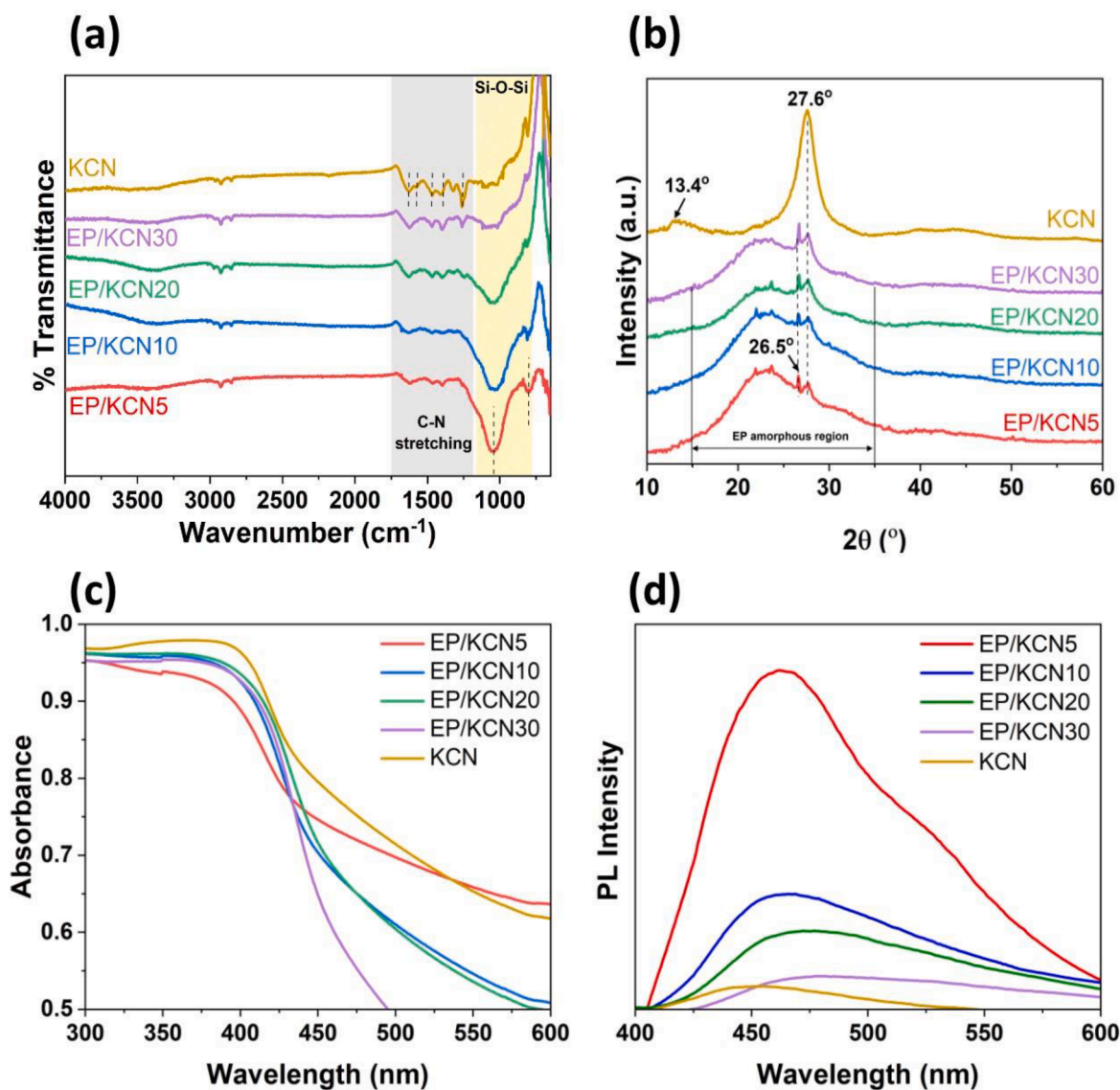


Fig. 2. (a) FTIR spectra, (b) XRD patterns, (c) UV-vis diffuse reflectance spectra, and (d) PL spectra (excitation at 355 nm) of EP and EP/KCN composites.

influence of precursor-to-support ratios on surface area [40].

XPS analysis was conducted to examine the chemical composition of the EP/KCN20 composite (Fig. S9). The elemental composition confirmed the presence of C, N, O, Si, K, and Al with concentrations of 36.41 %, 23.22 %, 20.39 %, 9.41 %, 9.17 %, and 1.39 %, respectively, suggesting the successful incorporation of all elements from both KCN and EP. The C 1s spectrum displayed core-level peaks at 284.6 eV, 286.3 eV, and 288.0 eV, corresponding to sp^2 -hybridized carbon atoms (C-C), C-O, and N-C=N bonds within nitrogen-containing aromatic rings [63]. The N 1s showed peaks at 398.5 eV for sp^2 -bonded nitrogen (N-C=N) and 400.4 eV for N-C₃ bonds [64]. Successful K-doping was confirmed by the K 2p spectrum, which showed characteristic peaks for K 2p_{3/2} at 293.2 eV and K 2p_{1/2} at 295.9 eV, indicating the formation of K-N and K-C bonds [65].

3.2. Photocatalytic degradation performance of EP/KCN

3.2.1. Effects of light reflection on photocatalytic activity

The influence of light reflection on the catalytic performance of the composite was investigated by placing aluminum foil beneath the reactor, as shown in Fig. S1. In the experiment, 0.06 g of EP/KCN10 was added to 50 mL of DPG solution (1 mg/L). The glass reactor was tested

under two conditions: one with aluminum foil at the bottom and one without it. As anticipated, the presence of aluminum foil significantly enhanced photocatalytic degradation performance. The foil improved solar irradiation absorption and promoted a uniform light distribution across the composite surface, thereby increasing photocatalytic efficiency [66]. As illustrated in Fig. 3a, the degradation of DPG (1 mg/L) increased by 20.0 % in the presence of aluminum foil. The degradation rate constant, k , increased from 0.238 h^{-1} to 0.473 h^{-1} (Fig. 3b). This enhancement is largely attributed to the elevated production of $O_2^{\bullet-}$, which plays a crucial role in boosting photocatalytic activity. The scavenger test results with and without aluminum and using BQ further confirm this (Fig. S10).

3.2.2. Effect of composite amount on photocatalytic activity

The influence of composite dose on photocatalytic performance was systematically evaluated by varying the amount of EP/KCN10 added to the DPG solution (0.02, 0.06, and 0.10 g). Increasing the dose enhanced the number of active sites, leading to more efficient DPG degradation (Fig. 3c). The k values were 0.247, 0.473, and 0.698 h^{-1} for the 0.02 g, 0.06 g, and 0.10 g doses, respectively (Fig. 3d). While the 0.10 g dose achieved complete removal of DPG within 3 h, this was mainly attributed to adsorption rather than photocatalytic degradation. This

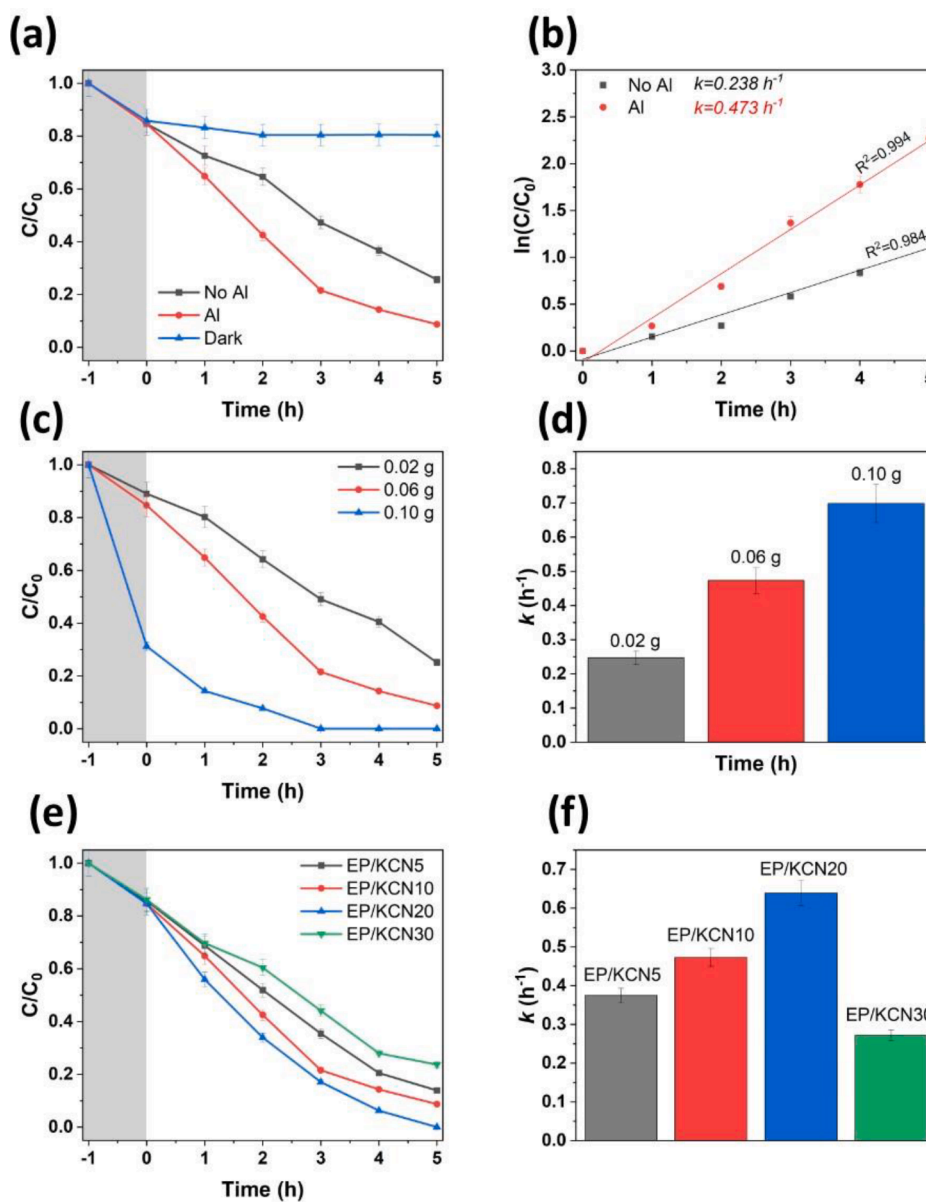


Fig. 3. Photocatalytic degradation curves of DPG under simulated solar irradiation and their corresponding degradation rate constants. (a, b) Effect of light reflection using EP/KCN10 (0.06 g), (c, d) Effect of composite dose with EP/KCN10, and (e, f) Effect of varying urea to EP ratio (0.06 g). Conditions: [DPG] = 1 mg/L, irradiation time = 5h, EP size = 1–2 mm.

phenomenon aligns with previous reports indicating that higher photocatalyst dose increase both adsorption capacity and overall removal efficiency [67,68]. Under dark conditions, using 0.10 g EP/KCN20 achieved 70.0 % removal, compared to approximately 15.0 % for the lower doses, confirming that adsorption was the dominant mechanism at this concentration. Consequently, a dose of 0.06 g was selected for subsequent experiments, providing an optimal balance between adsorption and photocatalytic degradation.

3.2.3. Impact of KCN loading on photocatalytic performance

The effect of varying the urea to EP ratio on the photocatalytic performance was thoroughly investigated. At low KCN loadings such as in EP/KCN5, the composite displayed the lowest photocatalytic performance (Fig. 3e). This is likely due to insufficient CN coverage on the EP surface, limiting the number of active sites available for degradation. As the KCN content increases, a significant enhancement in photocatalytic performance is observed (Fig. 3f), with EP/KCN20 achieving the highest degradation rate and fastest reaction kinetics (0.640 h^{-1}). This is

consistent with our previous work, which highlighted the role of K-doping in improving photocatalytic efficiency [23]. However, at higher KCN loadings, such as EP/KCN30, performance declined, likely due to excessive KCN, which led to particle agglomeration and increased light scattering, as reported in several studies [69,70].

3.2.4. Influence of EP particle size on photocatalytic efficiency

The size of EP particles is another critical factor that influences both the performance and stability of the composite. Larger EP particles (>2 mm) showed lower photocatalytic efficiency (Fig. 4a) with a k value of 0.0109 h^{-1} using EP/KCN20 (Fig. 4b), likely due to their reduced surface area and less effective interaction with DPG. Conversely, smaller EP particles (0.60–1 mm) achieved nearly complete removal of DPG within 3 h under simulated solar irradiation and a rate constant of 0.0517 h^{-1} . However, these smaller particles faced challenges in floatability due to reduced pore size and KCN leaching, limiting their recyclability. Moreover, EP is usually supplied in larger particle sizes, with smaller sizes becoming less available as sieving progresses. Therefore, EP particles

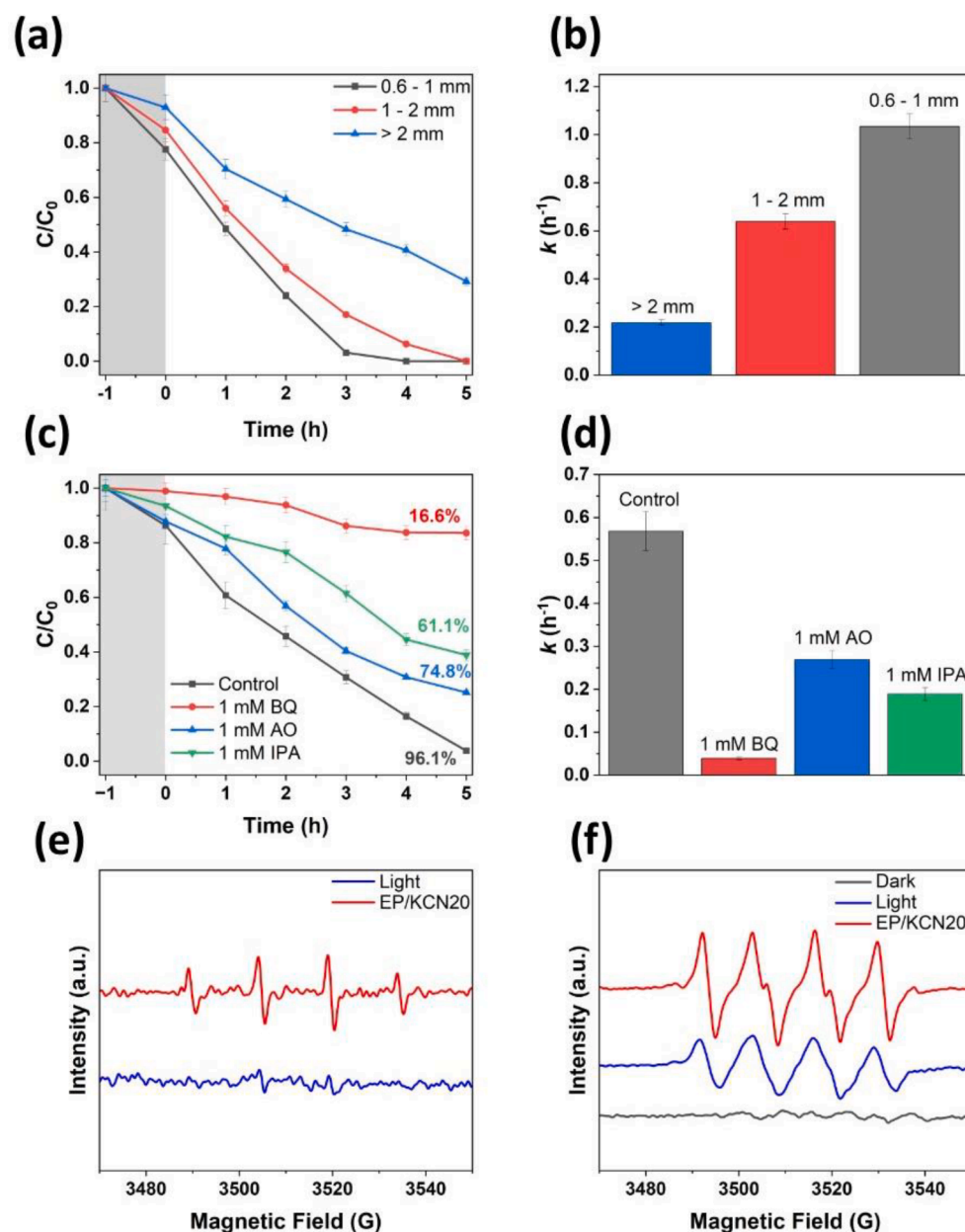


Fig. 4. (a) Photocatalytic degradation curves of DPG under simulated solar irradiation with varying perlite particle sizes, and (b) corresponding rate constants. (c) Scavenger tests using EP/KCN20 and (d) the corresponding rate constants. Conditions: [DPG] = 1 mg/L, irradiation time = 5h, composite dose = 0.06 g. (e, f) EPR tests for EP/KCN20 using DMPO in (e) water and (f) methanol.

sized 1–2 mm were selected for subsequent experiments as they offered an optimal balance of floatability, stability, and performance.

3.3. Identification of ROS in EP/KCN composites

Scavenger tests and EPR were performed to identify the main ROS involved in the photocatalytic degradation of DPG. Fig. 4c shows that the performance of EP/KCN20 (96.1 %) decreased by 80.0 % and the degradation rate slowed by a factor of 15 (Fig. 4d) with the addition of BQ, indicating that $O_2^{\bullet-}$ is the primary ROS responsible for DPG degradation. The efficiency was also slightly reduced with the addition of IPA, suggesting a minor role of $\bullet OH$. The addition of AO had the least impact on the scavengers tested, implying that h^+ plays a minimal role in the degradation process [71,72].

EPR measurements were also conducted to identify the radicals generated by the activation of the composite under irradiation. As

shown in Fig. 4e, the EPR spectrum of the DMPO aqueous solution with EP/KCN20 under light illumination exhibited a 1:2:2:1 pattern, characteristic of the DMPO- $\bullet OH$ adduct [66]. However, the presence of these spin adduct signals does not definitively indicate that EP/KCN20 directly generates $\bullet OH$. This observation may be attributed to the low stability of $O_2^{\bullet-}$ in water, potentially leading to the formation of $\bullet OH$ species, which produces the detected pattern. To specifically assess the generation of $O_2^{\bullet-}$, DMPO was also utilized in methanol. The EPR spectrum showed significantly higher intensity compared to the blank DMPO, indicating the generation of $O_2^{\bullet-}$ upon light irradiation (Fig. 4f).

3.4. Stability and recycling ability of EP/KCN composites

The durability of the EP/KCN20 composite was assessed across four consecutive cycles. After each 5-hour cycle, the composite was separated from the solution using a sieve, washed with ultrapure water, and dried

in an oven to prepare for reuse. During the initial cycle, EP/KCN20 demonstrated excellent photocatalytic performance, achieving a DPG degradation efficiency of over 96.0 %. By the fourth cycle, the degradation efficiency was maintained at 84.3 % (Fig. S11), indicating that the composite remains effective for multiple uses. This slight reduction in performance is likely due to the occupation of active sites by byproducts, which may hinder access to the catalytic sites without significantly affecting overall efficiency.

To gain further insights into the structural changes in the material after repeated use, EP/KCN20 was characterized post-recycling using FTIR and SEM. The FTIR spectra (Fig. S12) showed minimal variation, with a slight reduction in the intensity of the Si-O-Si stretching band between 800–1100 cm^{-1} , indicating minimal structural changes. SEM images (Fig. S13) also revealed a minor decrease in the surface coverage of KCN on the EP particles, suggesting a minimal loss of the active material after multiple cycles. Furthermore, the mass of EP/KCN20 was measured before and after each cycle, confirming nearly consistent weight across all cycles and indicating negligible material loss due to leaching.

3.5. Transformation products of DPG degradation

The transformation products formed during the degradation of DPG by EP/KCN20 were identified using mass formulas derived from TOF-MS (Figs. S14-S17). After 8 h of simulated solar irradiation, three main peaks with mass-to-charge ratios (m/z) of 136.084, 119.0609, and 210.1031 were detected, alongside the small DPG peak with m/z of 212.116 (Fig. 5). The molecular structures are compiled in Table S1. These findings align with previous studies [50,73,74], suggesting that the photocatalytic degradation of DPG by EP/KCN20 likely follows oxidative pathways under solar irradiation, leading to bond cleavage and the formation of smaller organic intermediates.

3.6. Performance in municipal wastewater and under natural solar light

Tire wear pollutants have been identified as a significant source of DPG contamination in aquatic environments, with concentrations typically ranging from hundreds of ng/L to a few $\mu\text{g/L}$ [75,76]. To evaluate the effectiveness of the EP/KCN20 photocatalytic system in mitigating this environmental issue, the composite was tested in a secondary effluent from a municipal wastewater treatment plant, spiked with 100 $\mu\text{g/L}$ DPG (black curve in Fig. 6), simulating a challenging contamination level similar to those found in real environmental matrices. Under

these conditions, EP/KCN20 achieved 85.6 % degradation of DPG within 5 h of simulated solar irradiation, slightly lower than in ultrapure water with 1 mg/L DPG. This lower efficiency is likely due to the presence of organic and inorganic constituents in the secondary effluent that can compete with DPG and consume ROS, thereby reducing the overall degradation efficiency. Nonetheless, the system demonstrates strong photocatalytic performance even under complex water matrices.

To better simulate practical wastewater treatment conditions, the system was tested at a slightly larger scale, with the volume increased tenfold while maintaining a DPG concentration of 100 $\mu\text{g/L}$ (red curve in Fig. 6). Additionally, to enhance the sustainability of the treatment, natural solar irradiation was used instead of simulated solar light, and the matrix was left unstirred to minimize additional energy inputs (Fig. S18). Under these conditions, DPG degradation in the 500 mL working volume reached 60.6 %, a promising outcome considering the scale-up and real-environmental conditions. The efficiency reduction compared to 85.6 % in lab-scale tests may be attributed to environmental variability, weather fluctuations, and the larger solution volume, which likely exacerbates mass transfer limitations [77]. To minimize these effects, the EP/KCN20 system would be best suited for application in shallow water bodies.

3.7. Comparison of EP/KCN with conventional supports

In contrast to powdered CN, which requires complex recovery processes such as filtration, the floatable EP/KCN20 composite allows for easy separation and reuse, making it particularly suitable for large-scale wastewater treatment [78,79]. Compared to conventional supports like melamine sponges [80,81], cellulose foams [82], or hydrogels [83], EP stands out due to its sustainability, as well as its chemical and thermal stability even under harsh conditions. Dispersed EP particles, unlike bulk supports, offer a greater surface area, enhancing photocatalyst deposition and increasing the exposure of active sites. This improvement in surface area contributes to better mass transfer and light penetration, thereby enhancing the interaction between the photocatalyst and contaminants.

Table S2 compares various floating supports for CN, highlighting the distinct advantages of EP. While other supports have shown effective photocatalytic degradation of contaminants in simple ultrapure water matrices, EP has demonstrated superior performance in complex, real wastewater conditions. EP's high efficiency, coupled with its environmental benefits and cost-effectiveness, positions it as an attractive choice for large-scale wastewater treatment. The next section will focus

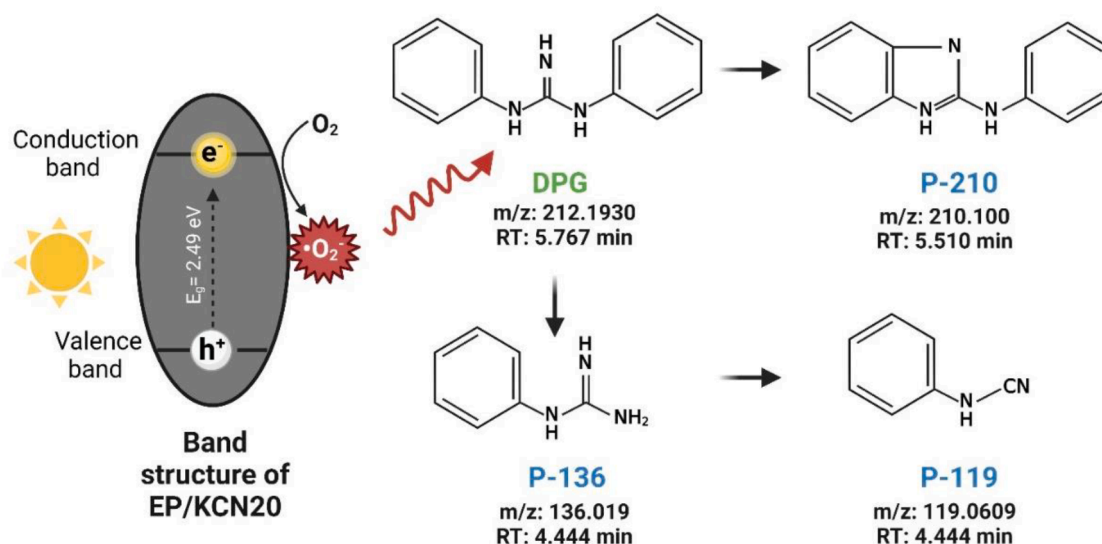


Fig. 5. Photocatalytic degradation of DPG using EP/KCN20 and the possible transformation products.

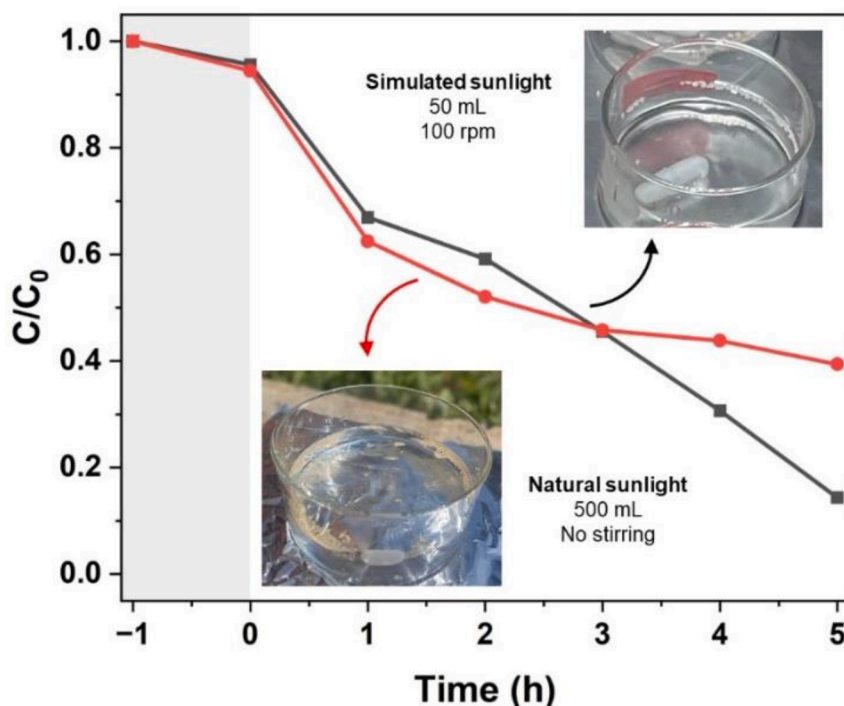


Fig. 6. Photocatalytic degradation curves of spiked DPG in secondary effluent under simulated solar irradiation (black curve) and natural solar irradiation (red curve) using EP/KCN20. (For interpretation of the references to colour in this figure legend, the reader is referred to the web version of this article.)

on evaluating the economic benefits of using EP in these applications.

3.8. Techno-economic analysis of EP/KCN system

The economic feasibility of the EP/KCN20 for wastewater treatment was evaluated using techno-economic analysis (TEA) that focuses on both capital expenditures (CAPEX) and operational expenditures (OPEX). The analysis was based on treating 100 m³ of wastewater per day, using the best experimental conditions from batch experiments: a dose of 1.2 g/L, a minimum of four cycles, each with a reaction time of 5 h. The system operates 8 h per day under natural solar irradiation, 5 days a week, for 300 days per year.

CAPEX is estimated at 40,000 USD, covering the muffle furnace for large-scale catalyst production and the reactor setup (including pipes, tanks, and other essential equipment). OPEX amounts to 163,505 USD/year, with raw materials (EP, urea, and KOH) accounting for 67.2 % of costs, labor 31.6 %, and electricity just 0.1 % due to minimal furnace usage and the absence of energy-intensive components such as artificial UV lamps or continuous stirring. Other operational costs include repair and maintenance, as well as water for catalyst washing and other general uses. Considering the amortized CAPEX, the total annualized cost for the system is approximately 167,356 USD/year, resulting in a treatment cost of 5.57 USD/m³. Reusing the catalyst for four cycles reduces operational costs by up to 30.0 %, primarily due to the reduced need for raw materials and lower waste disposal costs. Detailed breakdowns and formal calculations for the TEA are provided in **Text S1** and **Table S3**.

In contrast to traditional photocatalytic systems that often rely on UV lamps, stirring, or separation units, the EP/KCN20, coupled with natural solar irradiation, presents a more environmentally friendly alternative. Its cost is competitive, with most new technologies typically ranging from 2.60 to 30 USD/m³ in developing countries [84]. Recent studies have examined the economic feasibility of various photocatalytic systems. For instance, Demarema et al. [85] estimated the cost of using ZnO photocatalysts for wastewater treatment at 7.34 USD/m³, while Gar Alalm et al. [86] reported a cost of 9.71 USD/m³ for treating pesticide-

laden wastewater with TiO₂ photocatalysts. Not only is the EP/KCN20 system more cost-effective, but its floatability also simplifies recovery and reuse, unlike these conventional powdered photocatalysts. Furthermore, being composed of abundant materials and relying solely on solar energy positions EP/KCN20 as a superior eco-friendly option.

Despite these advantages, reducing operational costs remains a key challenge, particularly due to low urea yields. Sourcing urea from renewable feedstocks, such as agricultural waste or urine, could significantly reduce these costs [87–89]. Additionally, optimizing catalyst performance through material modifications, co-catalyst integration, or improved experimental conditions may reduce urea requirements, further enhancing economic viability.

4. Conclusion

This study demonstrated the enhanced photocatalytic performance of EP/KCN composites for the degradation of DPG under simulated solar irradiation. The incorporation of aluminum foil beneath the reactor increased the degradation efficiency by 20.0 %, with nearly double the reaction rate constant. The KCN loading significantly influenced photocatalytic efficiency, with EP/KCN20 (20:1 urea to perlite) exhibiting the highest degradation rate ($k = 0.640 \text{ h}^{-1}$), while excessive KCN loading in EP/KCN30 led to performance decline due to agglomeration and increased light scattering. Particle size also played a crucial role, where EP particles in the range of 1–2 mm provided an optimal balance of surface area, floatability, and photocatalytic performance. EPR and scavenger tests confirmed that O₂⁻ was the dominant species responsible for DPG degradation. The stability and reusability of EP/KCN20 were assessed over four cycles, showing a slight decline in efficiency from 96.1 % in the first cycle to 84.3 % in the fourth. Structural characterization post-recycling indicated minimal loss of active material, with negligible weight loss and minor changes in FTIR and SEM analysis. More importantly, EP/KCN20 established high efficiency in treating real secondary effluent from municipal WWTP spiked with DPG under natural solar irradiation. The economic analysis revealed a competitive treatment cost of 5.57 USD/m³ of wastewater, further supporting the

feasibility of EP/KCN20 in large-scale applications. This study provides a solid approach to the application of a stable floatable photocatalyst for the sustainable treatment of municipal wastewater containing organic contaminants.

CRedit authorship contribution statement

Bouthaina Aoudi: Conceptualization, Methodology, Data curation, Visualization, Formal analysis, Writing – original draft. **Julide Kahkeci:** Formal analysis, Writing – review & editing. **Isaac Sánchez-Montes:** Supervision, Writing – review & editing. **Yaman Boluk:** Supervision, Conceptualization, Methodology, Project administration, Funding acquisition, Resources, Writing – review & editing. **Mohamed Gamal El-Din:** Supervision, Conceptualization, Methodology, Project administration, Funding acquisition, Resources, Writing – review & editing.

Declaration of competing interest

The authors declare that they have no known competing financial interests or personal relationships that could have appeared to influence the work reported in this paper.

Acknowledgment

As a part of the Future Energy Systems research initiative at the University of Alberta, Canada, this research was made possible in part by funding through the Canada First Research Excellence Fund. This work was supported by the Canada Research Chairs Program and the Natural Sciences and Engineering Research Council of Canada (NSERC) Discovery Grants Program (RGPIN-2020-04378 Yaman Boluk and RGPIN-2018-05882 Mohamed Gamal El-Din). Support from Alberta Innovates Bio Solutions, Canada, is also acknowledged. The authors thank the support from the Alberta Innovates Graduate Student Scholarship, Canada, the Canada Foundation for Innovation (CFI), the John R. Evans Leaders Fund, and the Alberta Economic Development and Trade (EDT) – Research Capacity Program (RCP). Special thanks to Dr. Lingling Yang for conducting part of the analysis. The authors would like to thank Prof. Siraki from the Department of Pharmaceutical Sciences, University of Alberta, Canada, for the EPR experiments and analysis.

Appendix A. Supplementary data

Supplementary data to this article can be found online at <https://doi.org/10.1016/j.seppur.2025.132523>.

References

- [1] S.O. Ganiyu, S. Sable, M. Gamal El-Din, Advanced oxidation processes for the degradation of dissolved organics in produced water: a review of process performance, degradation kinetics and pathway, *Chem. Eng. J.* 429 (2022) 132492, <https://doi.org/10.1016/j.cej.2021.132492>.
- [2] J. Wang, R. Zhuang, Degradation of antibiotics by advanced oxidation processes: an overview, *Sci. Total Environ.* 701 (2020) 135023, <https://doi.org/10.1016/j.scitotenv.2019.135023>.
- [3] H. Mokarizadeh, I. Sánchez-Montes, S. Paul, N.A.S. Hussain, K. Moghrabi, J. L. Stafford, M. Gamal El-Din, Solar-activated tin oxide photocatalysis for efficient naphthenic acids removal and toxicity reduction in oil sands process water, *J. Environ. Chem. Eng.* 12 (2024) 114168, <https://doi.org/10.1016/j.jece.2024.114168>.
- [4] Z. An, I. Sánchez-Montes, P. Chelme-Ayala, C. Chen, M. Gamal El-Din, Efficient degradation of naphthenic acids in water using a sustainable engineered biochar/ZnO composite under simulated solar light, *Chem. Eng. J.* 489 (2024) 151308, <https://doi.org/10.1016/j.cej.2024.151308>.
- [5] Q. Wang, Y. Li, F. Huang, S. Song, G. Ai, X. Xin, B. Zhao, Y. Zheng, Z. Zhang, Recent Advances in g-C₃N₄-based materials and their application in energy and environmental sustainability, *Molecules* 28 (2023) 432, <https://doi.org/10.3390/molecules28010432>.
- [6] S.K. Selvam, R.A. Kumar, S.N. Balasubramanian, P.S. Kumar, A. Muthukrishnaraj, S.S. Kalaivani, R. Vinayagam, R.S. Azarudeen, M.A.R. Ahamed, A. Harikrishnan, S. Josephine, G.A.G. Rangasamy, Recent advancements in the environmental significance of the graphitic carbon nitride-based materials, *Desalination Water Treat* 318 (2024) 100385, <https://doi.org/10.1016/j.dwt.2024.100385>.

- [7] X. Xu, X. Zhang, H. He, L. Dai, J. Hu, C. Si, Graphitic carbon nitride enters the scene: a promising versatile tool for biomedical applications, *Langmuir* (2024), <https://doi.org/10.1021/acs.langmuir.4c01714>.
- [8] C. Guan, J. Jiang, S. Pang, X. Chen, R.D. Webster, T.-T. Lim, Facile synthesis of pure g-C₃N₄ materials for peroxymonosulfate activation to degrade bisphenol a: effects of precursors and annealing ambience on catalytic oxidation, *Chem. Eng. J.* 387 (2020) 123726, <https://doi.org/10.1016/j.cej.2019.123726>.
- [9] H. Wang, Q. Li, S. Zhang, Z. Chen, W. Wang, G. Zhao, L. Zhuang, B. Hu, X. Wang, Visible-light-driven N₂-g-C₃N₄ as a highly stable and efficient photocatalyst for bisphenol A and Cr(VI) removal in binary systems, *Catal. Today* 335 (2019) 110–116, <https://doi.org/10.1016/j.cattod.2018.09.037>.
- [10] T.-T. Pham, E.W. Shin, Thermal formation effect of g-C₃N₄ structure on the visible light driven photocatalysis of g-C₃N₄/NiTiO₃ Z-scheme composite photocatalysts, *Appl. Surf. Sci.* 447 (2018) 757–766, <https://doi.org/10.1016/j.apsusc.2018.04.051>.
- [11] Y. Wang, S. Zhao, Y. Zhang, J. Fang, W. Chen, S. Yuan, Y. Zhou, Facile synthesis of self-assembled g-C₃N₄ with abundant nitrogen defects for photocatalytic hydrogen evolution, *ACS Sustain. Chem. Eng.* 6 (2018) 10200–10210, <https://doi.org/10.1021/acssuschemeng.8b01499>.
- [12] T.K.A. Nguyen, T.-T. Pham, B. Gendensuren, E.-S. Oh, E.W. Shin, Defect engineering of water-dispersible g-C₃N₄ photocatalysts by chemical oxidative etching of bulk g-C₃N₄ prepared in different calcination atmospheres, *J. Mater. Sci. Technol.* 103 (2022) 232–243, <https://doi.org/10.1016/j.jmst.2021.07.013>.
- [13] J. Meng, X. Zhang, Y. Liu, M. Ren, Y. Guo, X. Yang, Y. Yang, Engineering of graphitic carbon nitride with simultaneous potassium doping sites and nitrogen defects for notably enhanced photocatalytic oxidation performance, *Sci. Total Environ.* 796 (2021) 148946, <https://doi.org/10.1016/j.scitotenv.2021.148946>.
- [14] S. Wang, J. Zhan, K. Chen, A. Ali, L. Zeng, H. Zhao, W. Hu, L. Zhu, X. Xu, Potassium-doped g-C₃N₄ achieving efficient visible-light-driven CO₂ reduction, *ACS Sustain. Chem. Eng.* 8 (2020) 8214–8222, <https://doi.org/10.1021/acssuschemeng.0c01151>.
- [15] S. Hu, F. Li, Z. Fan, F. Wang, Y. Zhao, Z. Lv, Band gap-tunable potassium doped graphitic carbon nitride with enhanced mineralization ability, *Dalton Trans.* 44 (2015) 1084–1092, <https://doi.org/10.1039/C4DT02658F>.
- [16] A. Alaghamdard, K. Ghandi, A comprehensive review of graphitic carbon nitride (g-C₃N₄)–metal oxide-based nanocomposites: potential for photocatalysis and sensing, *Nanomaterials* 12 (2022) 294, <https://doi.org/10.3390/nano12020294>.
- [17] L. Guo, J. Gao, Q. Huang, X. Wang, Z. Li, M. Li, W. Zhou, Element engineering in graphitic carbon nitride photocatalysts, *Renew. Sustain. Energy Rev.* 199 (2024) 114482, <https://doi.org/10.1016/j.rser.2024.114482>.
- [18] J. Li, D. Wu, J. Iocozzia, H. Du, X. Liu, Y. Yuan, W. Zhou, Z. Li, Z. Xue, Z. Lin, Achieving efficient incorporation of π-electrons into graphitic carbon nitride for markedly improved hydrogen generation, *Angew. Chem.* 131 (2019) 2007–2011, <https://doi.org/10.1002/ange.201813117>.
- [19] L. Jiang, X. Yuan, Y. Pan, J. Liang, G. Zeng, Z. Wu, H. Wang, Doping of graphitic carbon nitride for photocatalysis: a review, *Appl. Catal B* 217 (2017) 388–406, <https://doi.org/10.1016/j.apcatb.2017.06.003>.
- [20] G. Liu, Z. Tang, X. Gu, N. Li, H. Lv, Y. Huang, Y. Zeng, M. Yuan, Q. Meng, Y. Zhou, C. Wang, Boosting photocatalytic nitrogen reduction to ammonia by dual defective C-N and K-doping sites on graphitic carbon nitride nanorod arrays, *Appl. Catal B* 317 (2022) 121752, <https://doi.org/10.1016/j.apcatb.2022.121752>.
- [21] Z. Du, W. An, S. Luo, S. Chen, Y. Fu, H. He, X. Shen, Effects of K-doping on the microstructure and photocatalytic performance of porous g-C₃N₄ nanosheets, *New J. Chem.* 47 (2023) 11986–11995, <https://doi.org/10.1039/D3NJ01194A>.
- [22] S. Sun, J. Li, J. Cui, X. Gou, Q. Yang, Y. Jiang, S. Liang, Z. Yang, Simultaneously engineering K-doping and exfoliation into graphitic carbon nitride (g-C₃N₄) for enhanced photocatalytic hydrogen production, *Int. J. Hydrogen Energy* 44 (2019) 778–787, <https://doi.org/10.1016/j.ijhydene.2018.11.019>.
- [23] B. Aoudi, J. Kahkeci, Y. Boluk, M. Gamal El-Din, Enhanced g-C₃N₄ for sustainable solar degradation of 1,3-diphenylguanidine (DPG) in wastewater: investigating the effects of precursor, temperature, and potassium doping, *Chem. Eng. J.* 487 (2024) 150665, <https://doi.org/10.1016/j.cej.2024.150665>.
- [24] A. Balakrishnan, S. Appunni, M. Chintala, D.-V.-N. Vo, Biopolymer-supported TiO₂ as a sustainable photocatalyst for wastewater treatment: a review, *Environ. Chem. Lett.* 20 (2022) 3071–3098, <https://doi.org/10.1007/s10311-022-01443-8>.
- [25] H.M. Ali, F. Arabpour Roghabadi, V. Ahmadi, Solid-supported photocatalysts for wastewater treatment: supports contribution in the photocatalysis process, *Sol. Energy* 255 (2023) 99–125, <https://doi.org/10.1016/j.solener.2023.03.032>.
- [26] B. Aoudi, Y. Boluk, M. Gamal El-Din, Recent advances and future perspective on nanocellulose-based materials in diverse water treatment applications, *Sci. Total Environ.* 843 (2022) 156903, <https://doi.org/10.1016/j.scitotenv.2022.156903>.
- [27] H. Bang Truong, X. Cuong Nguyen, J. Hur, Recent advances in g-C₃N₄-based photocatalysis for water treatment: magnetic and floating photocatalysts, and applications of machine-learning techniques, *J. Environ. Manage.* 345 (2023) 118895, <https://doi.org/10.1016/j.jenvman.2023.118895>.
- [28] A. Rana, A. Sudhaik, P. Raizada, V.-H. Nguyen, C. Xia, A.A. Parwaz Khan, S. Thakur, P. Nguyen-Tri, C.C. Nguyen, S.Y. Kim, Q. Van Le, P. Singh, Graphitic carbon nitride based immobilized and non-immobilized floating photocatalysts for environmental remediation, *Chemosphere* 297 (2022) 134229, <https://doi.org/10.1016/j.chemosphere.2022.134229>.
- [29] Y. Li, I. Sánchez-Montes, L. Yang, X. Zhang, M. Gamal El-Din, Floating ZnO nanoparticles-coated micro glass bubbles for the efficient photodegradation of micropollutants in water, *Sep. Purif. Technol.* 342 (2024) 126933, <https://doi.org/10.1016/j.seppur.2024.126933>.
- [30] Z. Khoshraftar, H. Masoumi, A. Ghaemi, On the performance of perlite as a mineral adsorbent for heavy metals ions and dye removal from industrial wastewater: a

- review of the state of the art, *Case Stud. Chem. Environ. Eng.* 8 (2023) 100385, <https://doi.org/10.1016/j.csee.2023.100385>.
- [31] Z. Xing, J. Zhang, J. Cui, J. Yin, T. Zhao, J. Kuang, Z. Xiu, N. Wan, W. Zhou, Recent advances in floating TiO₂-based photocatalysts for environmental application, *Appl. Catal B* 225 (2018) 452–467, <https://doi.org/10.1016/j.apcatb.2017.12.005>.
- [32] O. Gencel, O. Yavuz Bayraktar, G. Kaplan, O. Arslan, M. Nodehi, A. Benli, A. Gholampour, T. Ozbakkaloglu, Lightweight foam concrete containing expanded perlite and glass sand: physico-mechanical, durability, and insulation properties, *Constr. Build. Mater.* 320 (2022) 126187, <https://doi.org/10.1016/j.conbuildmat.2021.126187>.
- [33] M.C. Acar, A.İ. Çelik, R. Kayabaşı, A. Şener, N. Özdöner, Y.O. Özkılıç, Production of perlite-based-aerated geopolymer using hydrogen peroxide as eco-friendly material for energy-efficient buildings, *J. Mater. Res. Technol.* 24 (2023) 81–99, <https://doi.org/10.1016/j.jmrt.2023.02.179>.
- [34] M. Długosz, P. Żmudzki, A. Kwiecień, K. Szczubińska, J. Krzek, M. Nowakowska, Photocatalytic degradation of sulfamethoxazole in aqueous solution using a floating TiO₂-expanded perlite photocatalyst, *J. Hazard. Mater.* 298 (2015) 146–153, <https://doi.org/10.1016/j.jhazmat.2015.05.016>.
- [35] J. Song, X. Wang, J. Ma, X. Wang, S. Xia, J. Zhao, Visible-light-driven in situ inactivation of *Microcystis aeruginosa* with the use of floating g-C₃N₄ heterojunction photocatalyst: performance, mechanisms and implications, *Appl. Catal B* 226 (2018) 83–92, <https://doi.org/10.1016/j.apcatb.2017.12.034>.
- [36] H.B. Truong, I. Rabani, B.T. Huy, N.H.T. Tran, J. Hur, Using floating photocatalyst mpg-C₃N₄/expanded perlite to treat natural organic matter under visible light, *Chem. Eng. J.* 466 (2023) 143178, <https://doi.org/10.1016/j.cej.2023.143178>.
- [37] C. Zhang, Y. Li, D. Shuai, W. Zhang, L. Niu, L. Wang, H. Zhang, Visible-light-driven, water-surface-floating antimicrobials developed from graphitic carbon nitride and expanded perlite for water disinfection, *Chemosphere* 208 (2018) 84–92, <https://doi.org/10.1016/j.chemosphere.2018.05.163>.
- [38] Y. Liu, X. Wang, Q. Sun, M. Yuan, Z. Sun, S. Xia, J. Zhao, Enhanced visible light photo-Fenton-like degradation of tetracycline by expanded perlite supported Fe₃O₄/g-C₃N₄ floating Z-scheme catalyst, *J. Hazard. Mater.* 424 (2022) 127387, <https://doi.org/10.1016/j.jhazmat.2021.127387>.
- [39] Q. Sun, X. Wang, Y. Liu, Y. Zhang, S. Xia, J. Zhao, Visible-light-driven g-C₃N₄ doped CuFe₂O₄ floating catalyst enhanced peroxydisulfate activation for sulfamethazine removal via singlet oxygen and high-valent metal-oxo species, *Chem. Eng. J.* 455 (2023) 140198, <https://doi.org/10.1016/j.cej.2023.140198>.
- [40] H. Chen, Y. Niu, H. Xu, S. Zhang, C. Huang, Z. Cui, Construction and investigation of graphitic carbon nitride/expanded perlite composite photocatalyst with floating ability, *Colloids Surf. A Physicochem. Eng. Asp.* 648 (2022) 129384, <https://doi.org/10.1016/j.colsurfa.2022.129384>.
- [41] S. Zhang, H. Li, Z. Yang, Synthesis, structural characterization and evaluation of a novel floating metal-free photocatalyst based on g-C₃N₄ grafted expanded perlite for the degradation of dyes, *Mater. Technol.* 33 (2018) 1–9, <https://doi.org/10.1080/10667857.2017.1367148>.
- [42] Y. Wang, X. Li, H. Yang, Y. Wu, Q. Pu, W. He, X. Li, A review of tire wear particles: occurrence, adverse effects, and control strategies, *Ecotoxicol. Environ. Saf.* 283 (2024) 116782, <https://doi.org/10.1016/j.ecoenv.2024.116782>.
- [43] B.J. Steira, R. Montes, A. Touffet, R. Rodil, R. Cela, H. Gallard, J.B. Quintana, Chlorination and bromination of 1,3-diphenylguanidine and 1,3-di-o-tolylguanidine: kinetics, transformation products and toxicity assessment, *J. Hazard. Mater.* 385 (2020) 121590, <https://doi.org/10.1016/j.jhazmat.2019.121590>.
- [44] M. Marques dos Santos, S.A. Snyder, Occurrence of polymer additives 1,3-diphenylguanidine (DPG), *N*-(1,3-Dimethylbutyl)-*N*'-phenyl-1,4-benzenediamine (6PPD), and chlorinated byproducts in drinking water: contribution from plumbing polymer materials, *Environ. Sci. Technol. Lett.* 10 (2023) 885–890, <https://doi.org/10.1021/acs.estlett.3c00446>.
- [45] Y. Wang, Y. Shuai, K. Chen, Diphenyl guanidine as vulcanization accelerators in sulfurized polyacrylonitrile for high performance lithium-sulfur battery, *Chem. Eng. J.* 388 (2020) 124378, <https://doi.org/10.1016/j.cej.2020.124378>.
- [46] Z.-M. Li, V.K. Pal, P. Kannan, W. Li, K. Kannan, 1,3-Diphenylguanidine, benzothiazole, benzotriazole, and their derivatives in soils collected from northeastern United States, *Sci. Total Environ.* 887 (2023) 164110, <https://doi.org/10.1016/j.scitotenv.2023.164110>.
- [47] Z.-M. Li, K. Kannan, Occurrence of 1,3-diphenylguanidine, 1,3-Di-o-tolylguanidine, and 1,2,3-triphenylguanidine in indoor dust from 11 Countries: implications for human exposure, *Environ. Sci. Tech.* 57 (2023) 6129–6138, <https://doi.org/10.1021/acs.est.3c00836>.
- [48] Z.-M. Li, K. Kannan, Mass loading, removal, and emission of 1,3-diphenylguanidine, benzotriazole, benzothiazole, *N*-(1,3-Dimethylbutyl)-*N*'-phenyl-*p*-phenylenediamine, and their derivatives in a wastewater treatment plant in New York State, USA, *ACS ES&T Water* 4 (2024) 2721–2730, <https://doi.org/10.1021/acsestwater.4c00221>.
- [49] T. Xiao, Z. Tang, Y. Yang, L. Tang, Y. Zhou, Z. Zou, In situ construction of hierarchical WO₃/g-C₃N₄ composite hollow microspheres as a Z-scheme photocatalyst for the degradation of antibiotics, *Appl. Catal B* 220 (2018) 417–428, <https://doi.org/10.1016/j.apcatb.2017.08.070>.
- [50] J. Kahkeci, B. Aoudi, I. Sánchez-Montes, M. Gamal El-Din, Engineered biochar supported bismuth tungstate: unveiling the influence of precursor concentrations and biochar dosage for the solar photocatalysis of 1,3-diphenylguanidine in secondary municipal effluent, *Chem. Eng. J.* 483 (2024) 149142, <https://doi.org/10.1016/j.cej.2024.149142>.
- [51] L. Meng, Z.T. How, S.O. Ganiyu, M. Gamal El-Din, Solar photocatalytic treatment of model and real oil sands process water naphthenic acids by bismuth tungstate: effect of catalyst morphology and cations on the degradation kinetics and pathways, *J. Hazard. Mater.* 413 (2021) 125396, <https://doi.org/10.1016/j.jhazmat.2021.125396>.
- [52] R. Huang, L. Yang, Z.T. How, Z. Fang, A. Bekele, D.J. Letinski, A.D. Redman, M. Gamal El-Din, Characterization of raw and ozonated oil sands process water utilizing atmospheric pressure gas chromatography time-of-flight mass spectrometry combined with solid phase microextraction, *Chemosphere* 266 (2021) 129017, <https://doi.org/10.1016/j.chemosphere.2020.129017>.
- [53] Natural Resources Canada. (2024). Photovoltaic potential and solar resource maps of Canada. Retrieved September 16, 2024, from <https://natural-resources.canada.ca/energy/energy-sources-distribution/renewables/solar-photovoltaic-energy/tools-solar-photovoltaic-energy/photovoltaic-and-solar-resource-maps/18366>.
- [54] A.A. Reka, B. Pavlovski, K. Lisichkov, A. Jashari, B. Boev, I. Boev, M. Lazarova, V. Eskizeybek, A. Oral, G. Jovanovski, P. Makreski, Chemical, mineralogical and structural features of native and expanded perlite from Macedonia, *Geologia Croatica* 72 (2019) 215–221, <https://doi.org/10.4154/gc.2019.18>.
- [55] R. Ebadollahi, S. Jafarirad, M. Kosari-Nasab, S. Mahjouri, Effect of explant source, perlite nanoparticles and TiO₂/perlite nanocomposites on phytochemical composition of metabolites in callus cultures of *Hypericum perforatum*, *Sci. Rep.* 9 (2019) 12998, <https://doi.org/10.1038/s41598-019-49504-3>.
- [56] M. Zhang, X. Bai, D. Liu, J. Wang, Y. Zhu, Enhanced catalytic activity of potassium-doped graphitic carbon nitride induced by lower valence position, *Appl. Catal B* 164 (2015) 77–81, <https://doi.org/10.1016/j.apcatb.2014.09.020>.
- [57] E. Dişçi, R. Polat, The influence of nano-CaO and nano-Al₂O₃ and curing conditions on perlite based geopolymer concrete produced by the one-part mixing method, *Constr. Build. Mater.* 346 (2022) 128484, <https://doi.org/10.1016/j.conbuildmat.2022.128484>.
- [58] O. Aksoy, E. Alyamac Seydibeyoglu, M. Mocan, M. Sutcu, N. Ozveren-Ucar, M. Seydibeyoglu, Characterization of perlite powders from Izmir, Türkiye region, *Physicochem. Probl. Miner. Process.* (2022), <https://doi.org/10.37190/ppmp/155277>.
- [59] S.M. Davachi, B.S. Heidari, R. Sahraeian, A. Abbaspourrad, The effect of nanoperlite and its silane treatment on the crystallinity, rheological, optical, and surface properties of polypropylene/nanoperlite nanocomposite films, *Compos. B* 175 (2019) 107088, <https://doi.org/10.1016/j.compositesb.2019.107088>.
- [60] S. Darvishi-Farash, M. Afsharpour, J. Heidarian, Novel siligraphene/g-C₃N₄ composites with enhanced visible light photocatalytic degradations of dyes and drugs, *Environ. Sci. Pollut. Res.* 28 (2021) 5938–5952, <https://doi.org/10.1007/s11356-020-10969-9>.
- [61] F. Darkhosh, M. Lashanizadegan, A.R. Mahjoub, A.H. Cheshme Khavar, One pot synthesis of CuFe₂O₄ @ expanding perlite as a novel efficient floating catalyst for rapid degradation of methylene blue under visible light illumination, *Solid State Sci.* 91 (2019) 61–72, <https://doi.org/10.1016/j.solidstatesciences.2019.03.009>.
- [62] I. do, N. Silva, E. Damasceno Júnior, J.M.F. Almeida, E.F. Dias, M.d. S.B. Silva, N. S. Fernandes, Experimental design for optimization of the photocatalytic degradation process of the remazol red dye by the TiO₂/expanded perlite composite, *Environ. Technol.* 42 (2021) 1493–1505, <https://doi.org/10.1080/09593330.2019.1672794>.
- [63] X. Yang, F. Qian, G. Zou, M. Li, J. Lu, Y. Li, M. Bao, Facile fabrication of acidified g-C₃N₄/g-C₃N₄ hybrids with enhanced photocatalysis performance under visible light irradiation, *Appl. Catal B* 193 (2016) 22–35, <https://doi.org/10.1016/j.apcatb.2016.03.060>.
- [64] J. Liu, W. Fang, Z. Wei, Z. Qin, Z. Jiang, W. Shangguan, Efficient photocatalytic hydrogen evolution on N-deficient g-C₃N₄ achieved by a molten salt post-treatment approach, *Appl. Catal B* 238 (2018) 465–470, <https://doi.org/10.1016/j.apcatb.2018.07.021>.
- [65] J. Yuan, N. Tian, Z. Zhu, W. Yu, M. Li, Y. Zhang, H. Huang, P, K doped crystalline g-C₃N₄ grafted with cyano groups for efficient visible-light-driven H₂O₂ evolution, *Chem. Eng. J.* 467 (2023) 143379, <https://doi.org/10.1016/j.cej.2023.143379>.
- [66] J. Ma, C. Wang, H. He, Enhanced photocatalytic oxidation of NO over g-C₃N₄-TiO₂ under UV and visible light, *Appl. Catal B* 184 (2016) 28–34, <https://doi.org/10.1016/j.apcatb.2015.11.013>.
- [67] U. Selengil, D. Yıldız, Investigation of the methylene blue adsorption onto waste perlite, desalination, *Water Treat* 262 (2022) 235–247, <https://doi.org/10.5004/dwt.2022.28530>.
- [68] N. Ghafourian, M. Lashanizadegan, S.N. Hosseini, Ag/TiO₂/EP: a low-cost and floating plasmonic photocatalyst for degrading furfural under visible light irradiation, *Int. J. Environ. Sci. Technol.* 14 (2017) 2721–2732, <https://doi.org/10.1007/s13762-017-1330-2>.
- [69] T.J. Al-Musawi, P. Rajiv, N. Mengelzadeh, F. Sadat Arghavan, D. Balarak, Photocatalytic efficiency of CuNiFe₂O₄ nanoparticles loaded on multi-walled carbon nanotubes as a novel photocatalyst for ampicillin degradation, *J. Mol. Liq.* 337 (2021) 116470, <https://doi.org/10.1016/j.molliq.2021.116470>.
- [70] F.S. Arghavan, T.J. Al-Musawi, E. Allahyari, M.H. Moslehi, N. Nasseh, A.H. Panahi, Complete degradation of tamoxifen using FeNi₃@SiO₂@ZnO as a photocatalyst with UV light irradiation: a study on the degradation process and sensitivity analysis using ANN tool, *Mater. Sci. Semicond. Process.* 128 (2021) 105725, <https://doi.org/10.1016/j.mssp.2021.105725>.
- [71] S. Li, G. Dong, R. Hailili, L. Yang, Y. Li, F. Wang, Y. Zeng, C. Wang, Effective photocatalytic H₂O₂ production under visible light irradiation at g-C₃N₄ modulated by carbon vacancies, *Appl. Catal B* 190 (2016) 26–35, <https://doi.org/10.1016/j.apcatb.2016.03.004>.
- [72] W.-D. Oh, L.-W. Lok, A. Veksha, A. Giannis, T.-T. Lim, Enhanced photocatalytic degradation of bisphenol A with Ag-decorated S-doped g-C₃N₄ under solar irradiation: performance and mechanistic studies, *Chem. Eng. J.* 333 (2018) 739–749, <https://doi.org/10.1016/j.cej.2017.09.182>.

- [73] J. Lai, T. Tang, X. Du, R. Wang, J. Liang, D. Song, Z. Dang, G. Lu, Oxidation of 1,3-diphenylguanidine (DPG) by goethite activated persulfate: mechanisms, products identification and reaction sites prediction, *Environ. Res.* 232 (2023) 116308, <https://doi.org/10.1016/j.envres.2023.116308>.
- [74] Investigation of transformation process of 1,3-diphenylguanidine in disinfection water treatment, Nanyang Technological University, 2023. <https://doi.org/10.32657/10356/173728>.
- [75] D.H. Quiñones, P.M. Álvarez, A. Rey, F.J. Beltrán, Removal of emerging contaminants from municipal WWTP secondary effluents by solar photocatalytic ozonation, A Pilot-Scale Study, *Sep. Purif. Technol.* 149 (2015) 132–139, <https://doi.org/10.1016/j.seppur.2015.05.033>.
- [76] A.M. Chávez, D.H. Quiñones, A. Rey, F.J. Beltrán, P.M. Álvarez, Simulated solar photocatalytic ozonation of contaminants of emerging concern and effluent organic matter in secondary effluents by a reusable magnetic catalyst, *Chem. Eng. J.* 398 (2020) 125642, <https://doi.org/10.1016/j.cej.2020.125642>.
- [77] M. Faramarzipour, M. Vossoughi, M. Borghei, Photocatalytic degradation of furfural by titania nanoparticles in a floating-bed photoreactor, *Chem. Eng. J.* 146 (2009) 79–85, <https://doi.org/10.1016/j.cej.2008.05.033>.
- [78] K.N. Van, H.T. Huu, V.N. Nguyen Thi, T.L. Le Thi, D.H. Truong, T.T. Truong, N. N. Dao, V. Vo, D.L. Tran, Y. Vasseghian, Facile construction of S-scheme SnO₂/g-C₃N₄ photocatalyst for improved photoactivity, *Chemosphere* 289 (2022) 133120, <https://doi.org/10.1016/j.chemosphere.2021.133120>.
- [79] J. Tang, J. Wang, L. Tang, C. Feng, X. Zhu, Y. Yi, H. Feng, J. Yu, X. Ren, Preparation of floating porous g-C₃N₄ photocatalyst via a facile one-pot method for efficient photocatalytic elimination of tetracycline under visible light irradiation, *Chem. Eng. J.* 430 (2022) 132669, <https://doi.org/10.1016/j.cej.2021.132669>.
- [80] Y. Tang, W. Cui, S. Wang, F. Dong, Efficient photocatalytic NO removal with inhibited NO₂ formation and catalyst loss over sponge-supported and functionalized g-C₃N₄, *J. Hazard. Mater.* 465 (2024) 133323, <https://doi.org/10.1016/j.jhazmat.2023.133323>.
- [81] M. Taha, A. Khalid, M.G. Elmahgary, S.S. Medany, Y.A. Attia, Fabricating a 3D floating porous PDMS – Ag/AgBr decorated g-C₃N₄ nanocomposite sponge as a reusable visible light photocatalyst, *Sci. Rep.* 14 (2024) 4184, <https://doi.org/10.1038/s41598-024-54500-3>.
- [82] P.R. Anusuyadevi, A.V. Riazanova, M.S. Hedenqvist, A.J. Svagan, Floating photocatalysts for effluent refinement based on stable pickering cellulose foams and graphitic carbon nitride (g-C₃N₄), *ACS Omega* 5 (2020) 22411–22419, <https://doi.org/10.1021/acsomega.0c02872>.
- [83] G. Fan, B. Du, J. Zhou, Z. Yan, Y. You, J. Luo, Porous self-floating 3D Ag₂O/g-C₃N₄ hydrogel and photocatalytic inactivation of *Microcystis aeruginosa* under visible light, *Chem. Eng. J.* 404 (2021) 126509, <https://doi.org/10.1016/j.cej.2020.126509>.
- [84] A.S. Adeleye, J.R. Conway, K. Garner, Y. Huang, Y. Su, A.A. Keller, Engineered nanomaterials for water treatment and remediation: costs, benefits, and applicability, *Chem. Eng. J.* 286 (2016) 640–662, <https://doi.org/10.1016/j.cej.2015.10.105>.
- [85] S. Demarema, M. Nasr, S. Ookawara, A. Abdelhaleem, New insights into green synthesis of metal oxide based photocatalysts for photodegradation of organic pollutants: a bibliometric analysis and techno-economic evaluation, *J. Clean. Prod.* 463 (2024) 142679, <https://doi.org/10.1016/j.jclepro.2024.142679>.
- [86] M. Gar Alalm, A. Tawfik, S. Ookawara, Comparison of solar TiO₂ photocatalysis and solar photo-Fenton for treatment of pesticides industry wastewater: operational conditions, kinetics, and costs, *J. Water Process Eng.* 8 (2015) 55–63, <https://doi.org/10.1016/j.jwpe.2015.09.007>.
- [87] H. Zhang, L. Wang, J. Herle, F. Maréchal, U. Desideri, Techno-economic comparison of 100% renewable urea production processes, *Appl. Energy* 284 (2021) 116401, <https://doi.org/10.1016/j.apenergy.2020.116401>.
- [88] P. Simha, A. Zabaniotou, M. Ganesapillai, Continuous urea–nitrogen recycling from human urine: a step towards creating a human excreta based bio–economy, *J. Clean. Prod.* 172 (2018) 4152–4161, <https://doi.org/10.1016/j.jclepro.2017.01.062>.
- [89] A. Khan, A. Abbas, R. Dickson, Towards a low-carbon future: exploring green urea synthesis for sustainable agriculture, *Green Chem.* 26 (2024) 1551–1565, <https://doi.org/10.1039/D3GC03228K>.